



King Saud University

Arabian Journal of Chemistry

www.ksu.edu.sa  
www.sciencedirect.com



ORIGINAL ARTICLE

# Plasma-modified iron-doped $\text{Ni}_3\text{S}_2$ nanosheet arrays as efficient electrocatalysts for hydrogen evolution reaction



Yongjun Shen <sup>a,b,\*</sup>, Yin Chen <sup>b,1</sup>, Shuaikang Fang <sup>b,1</sup>, Jae Kwang Park <sup>c</sup>, Kun Feng <sup>b</sup>

<sup>a</sup> Research Center of Secondary Resources and Environment, School of Chemical Engineering and Materials, Changzhou Institute of Technology, Changzhou 213022, China

<sup>b</sup> School of Chemistry and Chemical Engineering, Nantong University, Nantong 226019, China

<sup>c</sup> Department of Civil and Environmental Engineering, University of Wisconsin–Madison, 1415 Engineering Drive, Madison, WI 53706, USA

Received 6 August 2022; accepted 27 September 2022

Available online 1 October 2022

KEYWORDS

$\text{Ni}_3\text{S}_2$ ;  
Hydrogen evolution reaction;  
Nanosheet array;  
Plasma;  
Iron doping

**Abstract** The development of efficient transition-metal catalysts for the hydrogen evolution reaction is significant to meeting global energy demands. In this study, to realize a high-performance electrocatalyst, we synthesize an Fe-doped  $\text{Ni}_3\text{S}_2$  nanosheet material in situ on 3D structured nickel foam via the hydrothermal sulfide method, and then modify it by the dielectric barrier discharge plasma technique. Combining Fe atom doping and plasma modification increases the electrochemical surface area, provides an abundance of active sites, optimizes the electronic structure, and accelerates the reaction kinetics, thereby improving catalytic activity. As a result, the PA@ $\text{Fe}_{1/4}\text{-Ni}_3\text{S}_2/\text{NF}$  catalyst exhibits excellent hydrogen evolution reaction activity, only requires ultra-low overpotentials to achieve a current density of  $10 \text{ mA cm}^{-2}$ , and exhibits excellent durability. This study proposes a novel method for rationally designing non-noble metal electrocatalysts.

© 2022 The Authors. Published by Elsevier B.V. on behalf of King Saud University. This is an open access article under the CC BY-NC-ND license (<http://creativecommons.org/licenses/by-nc-nd/4.0/>).

## 1. Introduction

The development of green and clean renewable energy is imperative to achieving carbon neutrality and meeting the growing demand for energy (Chen et al., 2022; Xu et al., 2016a, 2016b; Guo et al., 2022). Because it has high energy density, no secondary pollution, and extensive sources, hydrogen is considered a clean energy source (Jin et al., 2019; Santo et al., 2020; Chen et al., 2021a, 2021b). Compared to hydrogen production from fossil fuels, water electrolysis is an ideal hydrogen-production technology because it produces high-purity hydrogen via a safe preparation process with a stable yield (Irshad and Munichandraiah, 2017; Feng et al., 2021). The catalyst determines the overpotential as well as the reaction rate and efficiency of

\* Corresponding author.

E-mail address: [shenyj@czust.edu.cn](mailto:shenyj@czust.edu.cn) (Y. Shen).

<sup>1</sup> These authors have contributed equally to this work and considered as co-first authors.

Peer review under responsibility of King Saud University.



Production and hosting by Elsevier

electrocatalytic water splitting (Xing et al., 2020; Suen et al., 2017; Anantharaj et al., 2018; Karthick, et al., 2017). Pt, the most efficient catalyst for hydrogen evolution reaction (HER), cannot be utilized on a large scale owing to its high cost and scarcity (Sultana et al., 2022; Li et al., 2022a, 2022b). Therefore, the exploration of inexpensive, highly active, and stable transition metal electrocatalysts for HER is a current research challenge.

In recent years, sulfides (Yang et al., 2019; Zheng et al., 2018; Zhang et al., 2018a, 2018b, 2018c, 2018d, 2018e, 2018f, 2018g; Ahmed et al., 2022; Feng et al., 2016), phosphides (Li et al., 2022a, 2022b; Zhang et al., 2020; Wang et al., 2022), hydroxides (Shi et al., 2022; Zhao et al., 2022), oxides (Xie et al., 2021; Mooni et al., 2020), selenides (Pu et al., 2016; Xu et al., 2016a, 2016b), and carbides (Zhang et al., 2018a, 2018b, 2018c, 2018d, 2018e, 2018f, 2018g; Zhu et al., 2021) of transition metals have been widely used in water splitting and have yielded excellent results. Among them,  $\text{Ni}_3\text{S}_2$  exhibits unique metallic properties and excellent electrical conductivity owing to its unique Ni–Ni bond network (Zhang et al., 2018a, 2018b, 2018c, 2018d, 2018e, 2018f, 2018g; Wang et al., 2021). Therefore, it is considered one of the most promising electrocatalysts. However, the electrocatalytic activity of  $\text{Ni}_3\text{S}_2$  is much lower than that of Pt-based catalysts. Heteroatom doping has been observed to increase active sites, optimize the electronic structure, and modulate adsorption capacity (Jian et al., 2018; Li et al., 2018). This is because doping the catalyst with free-electron-rich metal heteroatoms can increase the density of free carriers near the Fermi energy level and promote charge separation, improving the catalytic activity (Li et al., 2020; Tang et al., 2017). Zhang et al. synthesized Mo-doped  $\text{Ni}_3\text{S}_2$  electrocatalysts via the solid-phase melting method. The aMo- $\text{Ni}_3\text{S}_2$  catalysts showed ultralow overpotentials (74 mV at 10 mA cm<sup>-2</sup>) and Tafel slopes (54 mV dec<sup>-1</sup>) as well as excellent stability. This is attributed to the enhanced adsorption capacity for HER intermediates by Mo doping (Zhang et al., 2018a, 2018b, 2018c, 2018d, 2018e, 2018f, 2018g). Ma et al. synthesized V-doped  $\text{Ni}_3\text{S}_2$  nanosheet arrays on carbon fiber cloth as excellent bifunctional electrocatalysts for water electrolysis. The excellent catalytic activity indicates that the successful doping of V accelerates the reaction kinetics (Ma et al., 2019). Chen et al. systematically investigated the catalytic performance of 10 transition-metal-atom-doped  $\text{Ni}_3\text{S}_2$  compounds, among which Mn- $\text{Ni}_3\text{S}_2$ , Fe- $\text{Ni}_3\text{S}_2$ , and Ru- $\text{Ni}_3\text{S}_2$  showed superior HER activity and low overpotential (Chen et al., 2021a, 2021b). Furthermore, the direct growth of  $\text{Ni}_3\text{S}_2$  on nickel foam with a 3D structure enhances conductivity and promotes electron transport, thereby improving HER performance (Zhang et al., 2019).

In addition to elemental doping, researchers have improved the catalytic performance of materials via structural modifications, defect engineering, and crystal-plane control (Zhang et al., 2018a, 2018b, 2018c, 2018d, 2018e, 2018f, 2018g). For example, Zhang et al. (2018a, 2018b, 2018c, 2018d, 2018e, 2018f, 2018g) prepared NiO nanorods with oxygen vacancies by cation exchange, and the calculated partial density of states showed that the formation of new electronic states near the Fermi energy level enhanced the electrical conductivity of NiO. As a result, NiO had an ultra-high HER activity with a low overpotential of only 110 mV at 10 mA cm<sup>-2</sup>. A Ni-ZIF/Ni-B@NF bifunctional electrolytic water-splitting catalyst with a crystalline-amorphous mixed phase was developed (Xu et al., 2020). In alkaline solution, Ni-ZIF/Ni-B nanosheets loaded on NF required a hydrogen precipitation reaction overpotential of 67 mV and oxygen precipitation reaction overpotential of 234 mV to achieve a current density of 10 mA cm<sup>-2</sup>. The use of plasma technology provides many advantages for catalyst modification, such as high efficiency, unconventional preparation strategies, strong functionalization, and environmental friendliness (Liang et al., 2016; Wang et al., 2017; Jin et al., 2017). Plasma-technology-based methods can effectively remove the depletion layer at the interface and expose more surface sites for continuous charge transfer. Most importantly, plasma technology enables the surface modification of a material without destroying its inherent properties and structure, further enhancing hydrogen evolution performance (Wang et al., 2018). However, there are few studies on the use of

plasma-modified catalysts for the HER and oxygen evolution reaction (OER). However, there are few studies on the use of plasma-modified catalysts for hydrogen evolution reaction and oxygen evolution reaction. In particular, plasma-modified Fe- $\text{Ni}_3\text{S}_2$ /NF nanosheet catalysts for electrocatalytic water splitting have not been reported. Therefore, we prepared highly active HER catalysts using a novel strategy combining elemental doping and plasma modification.

In this study, Fe- $\text{Ni}_3\text{S}_2$  nanosheets with varied Fe/Ni molar ratios (Fe- $\text{Ni}_3\text{S}_2$ /NF) and original  $\text{Ni}_3\text{S}_2$  ( $\text{Ni}_3\text{S}_2$ /NF) were synthesized on nickel foam as catalysts for HER using a two-step hydrothermal method, where nickel foam provided the nickel source for  $\text{Ni}_3\text{S}_2$ . Subsequently, the  $\text{Fe}_{1/4}\text{-Ni}_3\text{S}_2$ /NF nanosheets with optimal catalytic activity were modified by DBD plasma. The PA@ $\text{Fe}_{1/4}\text{-Ni}_3\text{S}_2$ /NF nanosheet array displayed outstanding HER performance in alkaline solutions and excellent durability owing to the synthesis of Fe-doped  $\text{Ni}_3\text{S}_2$  directly on nickel foam to form sphere-like 3D nanosheet structures. This is mainly attributed to the doping of Fe atoms and the plasma modification exposing more active sites, increasing both the electrochemical active specific surface area and electron transfer rate. Therefore, this study not only provides a superior HER electrocatalyst, but also a new design strategy for high-performance catalysts.

## 2. Experimental section

### 2.1. Sample preparation

Deionized water with a resistivity of 18.2 MΩ cm<sup>-1</sup> was used throughout the experiment. Nickel nitrate hexahydrate (Ni (NO<sub>3</sub>)<sub>2</sub>·6H<sub>2</sub>O, 98 %), nickel foam (NF, 99 %), iron nitrate nonahydrate (Fe(NO<sub>3</sub>)<sub>3</sub>·9H<sub>2</sub>O, 99 %), and ammonium fluoride (NH<sub>4</sub>F, 99 %) were purchased from Aladdin (Shanghai, China). Urea (CH<sub>4</sub>N<sub>2</sub>O, 99 %) was purchased from Rhawn (Shanghai, China). All compounds were used directly in the experiment without further purification.

Several nickel foams measuring 2 cm × 3 cm were successively placed in 3 M HCl, anhydrous ethanol, and water for ultrasonic treatment for 15 min, and then vacuum dried at 60 °C.

The Fe- $\text{Ni}_3\text{S}_2$ /NF nanosheet was prepared using a simple two-step hydrothermal method. In the first step, to synthesize FeNi precursor/NF, a certain amount of nickel nitrate hexahydrate, iron nitrate nonahydrate, 4 mmol ammonium fluoride, and 10 mmol urea were added to 40 mL of water. After stirring until completely dissolved, the solution was transferred to a 50-mL Teflon-lined autoclave, and the processed NF was vertically placed in the solution. Subsequently, the solution was heated to 120 °C and processed at this temperature for 6 h. After cooling, NF loaded with FeNi precursors was sequentially washed with anhydrous ethanol and water, then dried at 60 °C. The mole ratios of Fe and Ni additions and their corresponding names are presented in Table 1. Meanwhile, Fe salt was removed during the synthesis to obtain a separate Ni precursor/NF. In the second step, to sulfide the NiFe precursor/NF, 8 mmol of Na<sub>2</sub>S was added to 40 mL of deionized water. Subsequently, the equipped Na<sub>2</sub>S solution was added to the autoclave containing FeNi precursor/NF, heated to 100 °C, and treated for 8 h at this temperature. After natural cooling, the sulfided product (Fe- $\text{Ni}_3\text{S}_2$ /NF) was retrieved, washed several times, then dried under vacuum at 60 °C. The Ni precursor/NF without Fe salt was sulfided via the same method to obtain the corresponding product ( $\text{Ni}_3\text{S}_2$ /NF).

The obtained Fe- $\text{Ni}_3\text{S}_2$ /NF catalyst was placed in the quartz reaction kettle (DBD-100B, Nanjing Suman Electronics

**Table 1** The Fe/Ni feed ratio for Fe-doped Ni<sub>3</sub>S<sub>2</sub>/NF with various Fe content.

Fe-doped Ni <sub>3</sub> S <sub>2</sub>	Fe(NO <sub>3</sub> ) <sub>3</sub> /Ni(NO <sub>3</sub> ) <sub>2</sub> feed ratio (mol/mol)
Fe <sub>1/10</sub> - Ni <sub>3</sub> S <sub>2</sub> /NF	1:10
Fe <sub>1/8</sub> - Ni <sub>3</sub> S <sub>2</sub> /NF	1:8
Fe <sub>1/4</sub> - Ni <sub>3</sub> S <sub>2</sub> /NF	1:4

Co., Ltd., China). The aluminum electrodes on both sides of the reaction kettle were exposed, and a filamentary discharge occurred. The input power of the system was mutually regulated using a circumscribed voltage regulator and a plasma generator (CTP-2000 K, Nanjing Suman Electronics Co., Ltd., China). After switching on the power, the input current (1A) and voltage (70 V) were adjusted to discharge the plate. We used this plasma device to modify catalysts for photocatalytic degradation of dyes (Shen et al., 2019; Xu et al., 2021). The samples were treated with air plasma to obtain plasma-modified Fe-Ni<sub>3</sub>S<sub>2</sub>/NF, marked as PA@ Fe-Ni<sub>3</sub>S<sub>2</sub>/NF.

## 2.2. Material characterization

The phase of the composite was determined using an X-ray diffractometer (Bruker D8 Advanced), which used Cu K radiation at a scanning speed of 5° min<sup>-1</sup>, with 2θ ranging from 10 to 90°. Field emission scanning electron microscopy (FESEM, ZEISS Gemini SEM 300), transmission electron microscopy (TEM, Tecnai G2 F20), and energy dispersive spectrometer (EDS) element mapping were used to examine the morphology and microstructure of the materials. The Thermo K-Alpha photoelectron spectrometer was used to obtain the X-ray photoelectron spectroscopy (XPS) spectra to identify the surface chemical characteristics and composition of the samples.

## 2.3. Electrochemical measurements

Electrochemical testing of as-prepared materials was performed using a conventional three-electrode setup with an electrochemical workstation (CHI 660E) in 1 M KOH electrolyte. Ag/AgCl, a carbon rod, and the as-prepared catalyst were employed as the reference, counter, and working electrodes, respectively. With 85 % iR correction, all original data were calibrated. For uniform comparison, all potentials in this study were converted to reversible hydrogen electrode (RHE) potentials by the standard formula. Before recording, the catalyst was scanned multiple times at 100 mV s<sup>-1</sup> until a steady image was obtained. The polarization curves of the catalysts were obtained at a scan rate of 0.005 V s<sup>-1</sup>. The overpotential versus log (J) was plotted in the LSV curve to get the Tafel slope. Electrochemical impedance spectroscopy (EIS) for HER was conducted under - 1.51 V vs RHE with a frequency range of 0.01 to 10<sup>5</sup> Hz. We evaluated the electrochemical capacitance (C<sub>d</sub>) using C<sub>vs</sub> with potentials ranging from 0.223 to 0.123 V vs RHE at scan speeds of 20, 40, 60, 80, and 100 mV s<sup>-1</sup> to determine the effective electrochemical surface area (ECSA) of the produced catalysts. Moreover, chronoamperometric response tests and the LSV curve after 1000 CV cycles were performed to investigate the durability of the samples.

## 3. Results and discussion

A two-step route was adapted to prepare the Fe-Ni<sub>3</sub>S<sub>2</sub>/NF composite, as illustrated in Fig. 1. To remove surface impurities, the 3D structured nickel foam was treated with 3 M HCl, anhydrous ethanol, and deionized water for 5 min, and then used directly as a catalyst carrier. FeNi precursor/NF was prepared using a facile hydrothermal treatment by adding NF to the aqueous solution of Ni(NO<sub>3</sub>)<sub>2</sub>·6H<sub>2</sub>O, NH<sub>4</sub>F, Fe (NO<sub>3</sub>)<sub>3</sub>·9H<sub>2</sub>O, and CH<sub>4</sub>N<sub>2</sub>O; the color of Ni foam changed from silver to yellowish-green. It was then treated in a solution of Na<sub>2</sub>S, during which the OH<sup>-</sup> in the hydroxide was converted to sulfide by ion exchange with S<sup>2-</sup> to obtain Fe-Ni<sub>3</sub>S<sub>2</sub>/NF (Zhang et al., 2018a, 2018b, 2018c, 2018d, 2018e, 2018f, 2018g). The samples were treated with air plasma to obtain PA@Fe-Ni<sub>3</sub>S<sub>2</sub>/NF. Sample Ni<sub>3</sub>S<sub>2</sub>/NF was prepared as a control, following treatment similar to that of the Fe-Ni<sub>3</sub>S<sub>2</sub>/NF, but without using Fe salt precursors. The typical X-ray diffraction pattern of the prepared catalyst is shown in Fig. 2, demonstrating the detailed structural and phase information of the products. The diffraction peaks of 2θ = 21.7°, 31.1°, 37.7°, 49.7°, and 55.1° accurately correspond to the (101), (110), (003), (113), and (112) crystallographic planes of the hexagonal Ni<sub>3</sub>S<sub>2</sub> (JCPDS 44-1418), implying the successful formation of Ni<sub>3</sub>S<sub>2</sub>. Fe-Ni<sub>3</sub>S<sub>2</sub>/NF with different Fe/Ni molar ratios (Fe<sub>1/4</sub>-Ni<sub>3</sub>S<sub>2</sub>/NF, Fe<sub>1/8</sub>-Ni<sub>3</sub>S<sub>2</sub>/NF, Fe<sub>1/10</sub>-Ni<sub>3</sub>S<sub>2</sub>/NF) show XRD patterns similar to those of Ni<sub>3</sub>S<sub>2</sub>/NF, implying the absence of new phases. This indicates that the crystalline phases of Ni<sub>3</sub>S<sub>2</sub>/NF were not significantly changed by Fe doping, suggesting that no Fe sulfides were produced. The XRD pattern of PA@Fe<sub>1/4</sub>-Ni<sub>3</sub>S<sub>2</sub>/NF was similar to that before plasma modification, indicating that the plasma treatment did not change the crystal structure of the material. In addition, the diffraction peaks of both the Fe-doped Ni<sub>3</sub>S<sub>2</sub>/NF and plasma-modified Fe<sub>1/4</sub>-Ni<sub>3</sub>S<sub>2</sub>/NF were shifted by 0.04° in diffraction angle compared with that of the pristine Ni<sub>3</sub>S<sub>2</sub>. This indicates that the insertion of Fe<sup>3+</sup> ions can reduce lattice spacing, and proves that plasma treatment does not affect the crystal structure of the catalysts (Kim et al., 2017).

Scanning electron microscopy (SEM) was used to examine the morphology and microstructure of certain representative samples. As shown in Fig. 3a, the synthesis of pure Ni<sub>3</sub>S<sub>2</sub>/NF without the addition of iron to the reaction yielded Ni<sub>3</sub>S<sub>2</sub>/NF with an irregular sheet-like structure; the sheet-like structure was unclear and the distribution was not uniform. When the reaction condition is Fe/Ni = 1:10, Fe<sub>1/10</sub>-Ni<sub>3</sub>S<sub>2</sub>/NF and pristine Ni<sub>3</sub>S<sub>2</sub>/NF exhibit similar vertically arranged nanosheet structures (Fig. 3b). At reaction conditions of Fe/Ni = 1:8, the obtained Fe<sub>1/8</sub>-Ni<sub>3</sub>S<sub>2</sub>/NF samples showed a regular and dense nanosheet array structure (Fig. 3c-d). Interestingly, when the molar ratio of Fe/Ni was 1:4, the nanosheets began to agglomerate and staggered to form a spherical-like structure (Fig. 3e-f). As shown in Fig. 3g, the plasma-modified Fe<sub>1/8</sub>-Ni<sub>3</sub>S<sub>2</sub>/NF has a small amount of irregular spherical structure, and the rest maintain the nanosheet structure. After plasma modification of Fe<sub>1/4</sub>-Ni<sub>3</sub>S<sub>2</sub>/NF catalyst, the agglomerated nanosheets began to separate into flower spheres sequentially (Fig. 3h-i). Each flower sphere was composed of numerous nanosheets, which were firmly anchored on the Ni foam to form a very strong 3D structure, making PA@Fe<sub>1/4</sub>-Ni<sub>3</sub>S<sub>2</sub>/NF a robust and

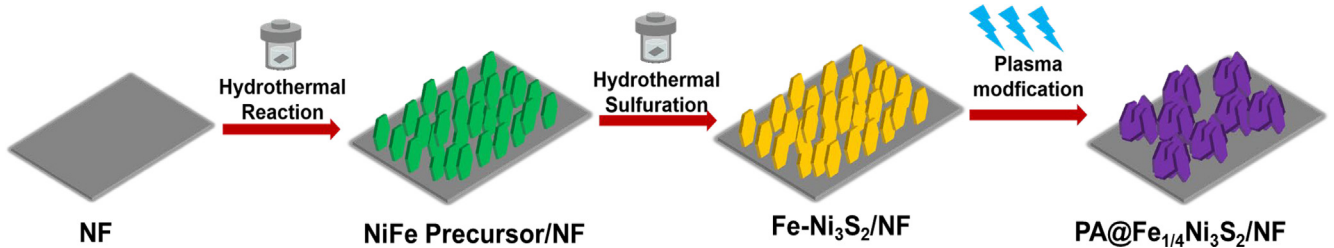


**Fig. 1** Schematic illustration of the preparation of the plasma-modified Fe<sub>1/4</sub>-Ni<sub>3</sub>S<sub>2</sub>/NF nanosheet arrays.

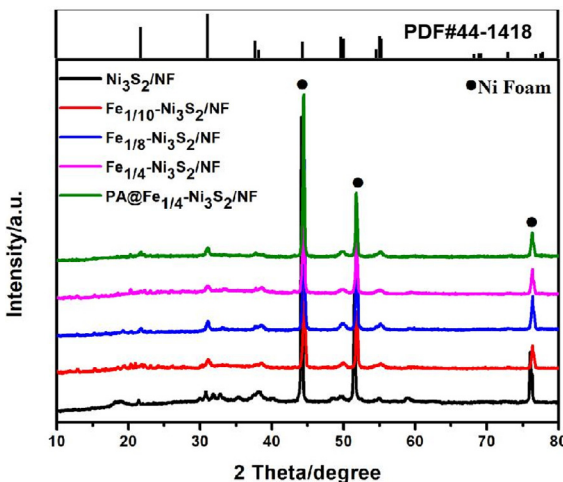


**Fig. 2** (a) XRD patterns of Ni<sub>3</sub>S<sub>2</sub>/NF, Fe<sub>1/10</sub>-Ni<sub>3</sub>S<sub>2</sub>/NF, Fe<sub>1/8</sub>-Ni<sub>3</sub>S<sub>2</sub>/NF, Fe<sub>1/4</sub>-Ni<sub>3</sub>S<sub>2</sub>/NF and PA@Fe<sub>1/4</sub>-Ni<sub>3</sub>S<sub>2</sub>/NF.

stable catalyst. Fig. 3j shows the EDS spectra of PA@Fe<sub>1/4</sub>-Ni<sub>3</sub>S<sub>2</sub>/NF, which identified Fe, Ni, and S in the composite, implying the successful preparation of the composites.

The morphology and structure of Fe<sub>1/4</sub>-Ni<sub>3</sub>S<sub>2</sub>/NF after plasma modification were also investigated using TEM. As shown in the TEM images (Fig. 4a), the PA@Fe<sub>1/4</sub>-Ni<sub>3</sub>S<sub>2</sub>/NF nanosheet was observed, consistent with the SEM results. The structure and properties of the materials were further studied using HRTEM images. The lattice fringes in Fig. 4b are very clear and easy to identify, which fully illustrates the remarkable crystallinity of PA@Fe<sub>1/4</sub>-Ni<sub>3</sub>S<sub>2</sub>/NF. Meanwhile, the HRTEM image of PA@Fe<sub>1/4</sub>-Ni<sub>3</sub>S<sub>2</sub>/NF exhibits four distinct lattice fringes of 0.29, 0.24, 0.23, and 0.18 nm, which correspond with the (110), (003), (021), and (113) lattice planes of the Ni<sub>3</sub>S<sub>2</sub>/NF sample, respectively. The exposure of these lattice planes contributes to the increase in the catalytic activity, which is essential for catalysts (Feng et al., 2015). The polycrystalline character of the nanosheets was verified by the corresponding-area electron diffraction (SAED) pattern, with the diffraction rings corresponding to the (113), (021), (003), and (110) planes of Ni<sub>3</sub>S<sub>2</sub>/NF (Fig. 4c), which was consistent with the XRD results. In addition, the high angle annular dark field (HAADF) scanning images and EDX clearly reveal that Fe, Ni, and S elements are uniformly distributed in PA@Fe<sub>1/4</sub>-Ni<sub>3</sub>S<sub>2</sub>/NF nanosheets (Fig. 4d-h).

The changes in surface composition before and after plasma treatment were also studied by XPS. As shown in Fig. 5a, the XPS full spectrum of PA@Fe<sub>1/4</sub>-Ni<sub>3</sub>S<sub>2</sub>/NF indicates the presence of Ni, Fe, O, and S elements, which is consistent with the EDX results. As shown in Fig. 5a, the XPS full spectrum of PA@Fe<sub>1/4</sub>-Ni<sub>3</sub>S<sub>2</sub>/NF indicates the presence of Ni, Fe, O, and S, which is consistent with the EDS results. Fig. 5b shows the high-resolution XP spectrum of the Fe 2p region, deconvoluted into two main peaks located at 711.9 eV and 724.9 eV, corresponding to the binding energies of Fe 2p<sub>3/2</sub> and Fe 2p<sub>1/2</sub>, respectively. These peaks are mainly attributed to Fe<sup>3+</sup> and are consistent with those observed in previous studies (Yuan et al., 2017; Cheng et al., 2015). This result strongly proves that iron was successfully doped into Ni<sub>3</sub>S<sub>2</sub>. The Ni<sup>3+</sup> and Ni<sup>2+</sup> regions were used to fit the two primary peaks. Ni<sup>3+</sup> and Ni<sup>2+</sup> have characteristic peaks in the Ni 2p<sub>3/2</sub> band at approximately 856.5 eV and 855.1 eV, respectively, whereas Ni<sup>2+</sup> and Ni<sup>3+</sup> have characteristic peaks in the Ni 2p<sub>1/2</sub> band at approximately 872.6 eV and 874.3 eV, respectively (Fig. 5c). Ni exists in the form of Ni<sup>2+</sup> and Ni<sup>3+</sup> in PA@Fe<sub>1/4</sub>-Ni<sub>3</sub>S<sub>2</sub>/NF nanosheets (Biesinger et al., 2009). The deconvolution of the S 2p spectra of PA@Fe<sub>1/4</sub>-Ni<sub>3</sub>S<sub>2</sub>/NF (Fig. 5d) shows two peaks. The two main peaks at 161.8 eV and 168.3 eV correspond to the Ni-S and S—O species, respectively, where the latter originates from sulfate species formed upon exposure to air (Dueso et al., 2012). The existence of S<sup>2-</sup> and the abundance of S vacancies in PA@Fe<sub>1/4</sub>-Ni<sub>3</sub>S<sub>2</sub>/NF was demonstrated (Zhang et al., 2018a, 2018b, 2018c, 2018d, 2018e, 2018f, 2018g; Lu et al., 2016). The deconvolution of the S 2p spectra of PA@Fe<sub>1/4</sub>-Ni<sub>3</sub>S<sub>2</sub>/NF (Fig. 5d) showed the presence of two peaks. The two main peaks at 161.8 eV and 168.3 eV correspond to the Ni-S and S—O species, respectively, the latter originating from sulfate species formed upon exposure to air (Dueso et al., 2012). The existence of S<sup>2-</sup> and the abundance of S vacancies in PA@Fe<sub>1/4</sub>-Ni<sub>3</sub>S<sub>2</sub>/NF were proved (Zhang et al., 2018a, 2018b, 2018c, 2018d, 2018e, 2018f, 2018g; Lu et al., 2016). These results indicate the successful doping of Fe in the PA@Fe<sub>1/4</sub>-Ni<sub>3</sub>S<sub>2</sub>/NF nanosheet arrays, and that the catalyst exposes abundant catalytic active sites, which can significantly improve the water-splitting performance.

In a conventional three-electrode system, we measure the hydrogen evolution activity of Ni<sub>3</sub>S<sub>2</sub>/NF, Fe<sub>1/10</sub>-Ni<sub>3</sub>S<sub>2</sub>/NF, Fe<sub>1/8</sub>-Ni<sub>3</sub>S<sub>2</sub>/NF, Fe<sub>1/4</sub>-Ni<sub>3</sub>S<sub>2</sub>/NF, and plasma-modified Fe<sub>1/4</sub>-Ni<sub>3</sub>S<sub>2</sub>/NF. The linear sweep voltammetry (LSV) curves of the catalyst and the corresponding overpotential are shown in Fig. 6a and 6b, with the current density normalized by geometric surface area (1 cm<sup>2</sup>). Compared to the other samples, PA@Fe<sub>1/4</sub>-Ni<sub>3</sub>S<sub>2</sub>/NF clearly has a lower onset potential and substantially higher current density at the same potential.

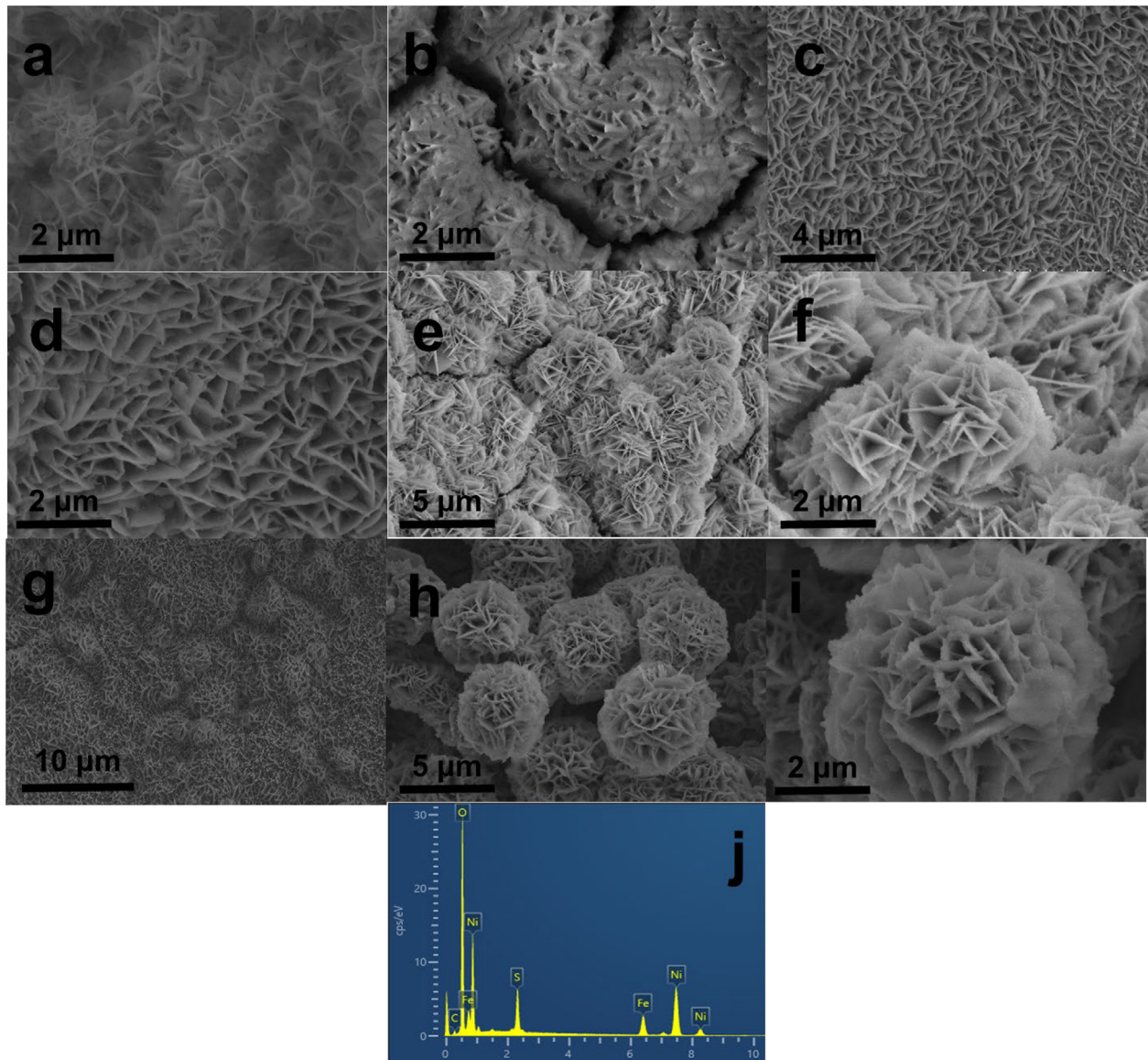


**Fig. 3** SEM images of (a) Ni<sub>3</sub>S<sub>2</sub>/NF, (b) Fe<sub>1/10</sub>-Ni<sub>3</sub>S<sub>2</sub>/NF, (c-d) Fe<sub>1/8</sub>-Ni<sub>3</sub>S<sub>2</sub>/NF, (e-f) Fe<sub>1/4</sub>-Ni<sub>3</sub>S<sub>2</sub>/NF, (g)PA@Fe<sub>1/4</sub>-Ni<sub>3</sub>S<sub>2</sub>/NF, (h-i) PA@Fe<sub>1/4</sub>-Ni<sub>3</sub>S<sub>2</sub>/NF. (j) EDX spectrum of PA@Fe<sub>1/4</sub>-Ni<sub>3</sub>S<sub>2</sub>/NF nanosheet arrays.

Similarly, PA@Fe<sub>1/4</sub>-Ni<sub>3</sub>S<sub>2</sub>/NF has a substantially greater current density than other materials at the same potential. Furthermore, compared to Fe<sub>1/4</sub>-Ni<sub>3</sub>S<sub>2</sub>/NF (111 mV), Fe<sub>1/8</sub>-Ni<sub>3</sub>S<sub>2</sub>/NF (131 mV), Fe<sub>1/10</sub>-Ni<sub>3</sub>S<sub>2</sub>/NF (139 mV), and Ni<sub>3</sub>S<sub>2</sub> / NF (217 mV), PA@Fe<sub>1/4</sub>-Ni<sub>3</sub>S<sub>2</sub>/NF exhibits high electrocatalytic activity, with only 91 mV of overpotential at 10 mA cm<sup>-2</sup>. Compared with previously reported Pt/C electrocatalysts (Yu et al., 2017; Zheng et al., 2019), PA@Fe<sub>1/4</sub>-Ni<sub>3</sub>S<sub>2</sub>/NF has a slightly higher overpotential, but higher HER performance than that of most reported Ni-based sulfides (Li et al., 2013; Zhou et al., 2020; Hao et al., 2020). Compared with Pt/C electrocatalysts in other literatures, the PA@Fe<sub>1/4</sub>-Ni<sub>3</sub>S<sub>2</sub>/NF catalyst has a slightly higher overpotential. The results show that the electrocatalytic performance of the catalyst increases as the Fe/Ni molar ratio increases, and the plasma modification further improves catalytic performance.

In addition, we compared the PA@Fe<sub>1/4</sub>-Ni<sub>3</sub>S<sub>2</sub>/NF catalyst with related nickel-based sulfides. Lee et al. prepared

H-CoS<sub>x</sub>@NiFe LDH/NF catalysts with a unique structure by electrodeposition; the optimized heterogeneous structure provided sufficient active sites and facilitated electrolyte penetration (Lee and Park, 2022). In alkaline solutions, this catalyst had excellent performance for the HER and OER with ultra-low overpotentials of 99 and 250 mV, respectively. Jia et al. (2021) fabricated novel Ni<sub>3</sub>S<sub>2</sub>/Cu–NiCo LDH heterostructured nanosheet catalysts on 3D NF carriers by a two-step hydrothermal method, in which doping with Cu ions and Ni<sub>3</sub>S<sub>2</sub> modified the microstructure and electronic structure, resulting in excellent catalytic performance. The optimized Ni<sub>3</sub>S<sub>2</sub>/Cu–NiCo LDH/NF had excellent durability, with overpotentials of 156 and 304 mV at current densities of 10 and 100 mA cm<sup>-2</sup>, respectively. Zhou et al. (2020) synthesized a heterojunction material of Co<sub>9</sub>S<sub>8</sub> vertically aligned on Ni<sub>3</sub>S<sub>2</sub> spheres by a one-step hydrothermal method, resulting in Co<sub>9</sub>-S<sub>8</sub>@Ni<sub>3</sub>S<sub>2</sub> with excellent HER activity (a current density of 10 mA cm<sup>-2</sup> with an overpotential of only 160 mV). In

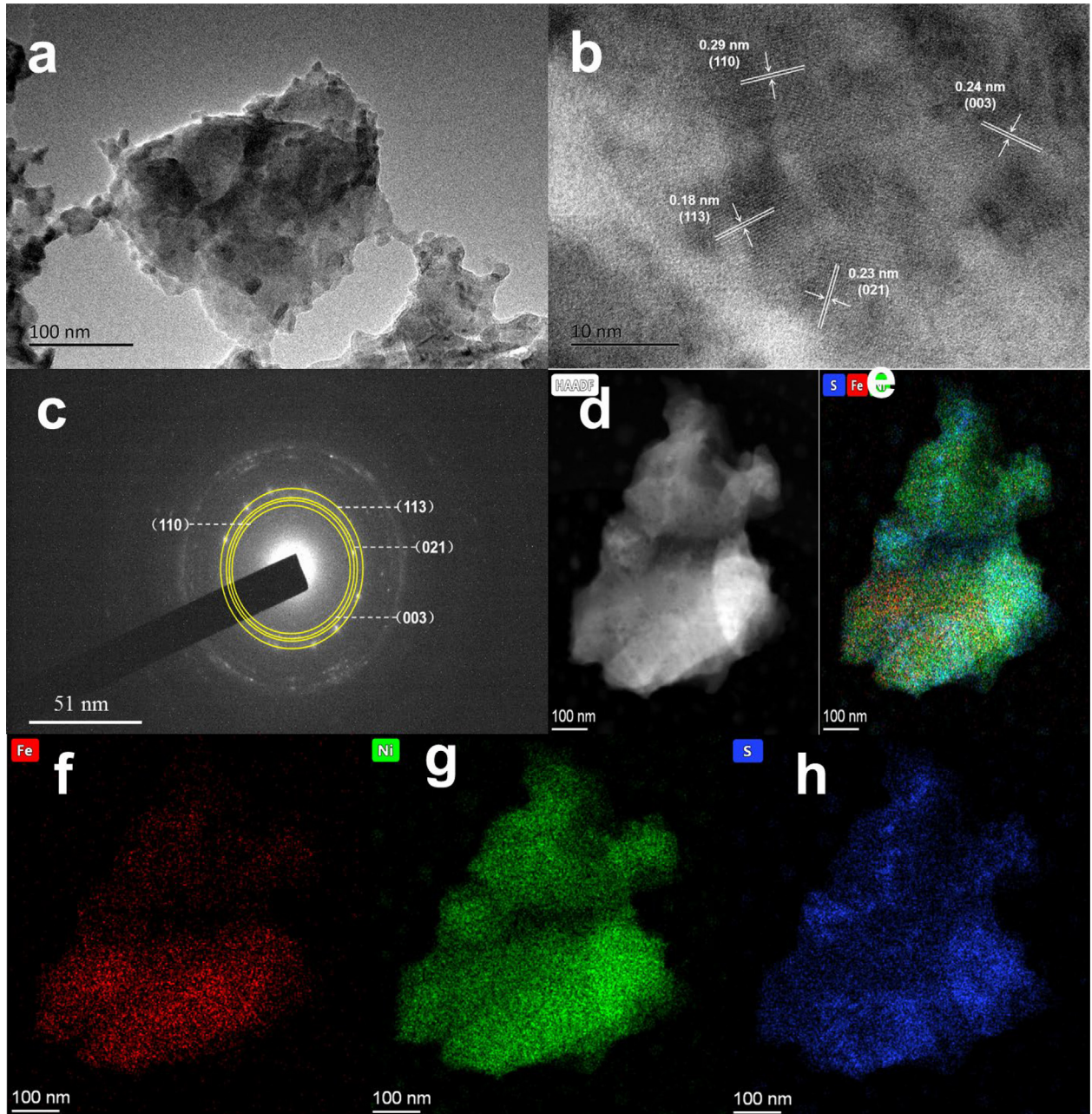


**Fig. 4** (a) TEM image of PA@Fe<sub>1/4</sub>-Ni<sub>3</sub>S<sub>2</sub>/NF nanosheet. (b) The high-resolution TEM image of PA@Fe<sub>1/4</sub>-Ni<sub>3</sub>S<sub>2</sub>/NF nanosheet. (c) SAED pattern of PA@Fe<sub>1/4</sub>-Ni<sub>3</sub>S<sub>2</sub>/NF nanosheet. (d-h) The HADDF image and EDX mapping of Fe, Ni and S from PA@Fe<sub>1/4</sub>-Ni<sub>3</sub>S<sub>2</sub>/NF nanosheet.

addition, electrocatalytic urea splitting is an effective hydrogen-production process. Liu et al. (2021) prepared (Ni<sub>x</sub>-Fe<sub>1-x</sub>)<sub>3</sub>S<sub>2</sub>/NF nanosheets by a simple hydrothermal method, and the material showed the highest activity for the HER and urea oxidation reaction at a 0.25/0.75 M ratio of Ni/Fe. (Ni<sub>0.25</sub>Fe<sub>0.75</sub>)<sub>3</sub>S<sub>2</sub>/NF required an overpotential of only 93 mV at a current density of 10 mA cm<sup>-2</sup> to drive the HER. Compared with these electrocatalysts, the plasma-modified PA@Fe<sub>1/4</sub>-Ni<sub>3</sub>S<sub>2</sub>/NF catalyst developed in this study exhibits higher performance, with an overpotential of only 91 mV.

To understand the HER kinetics, Tafel plots of all modified electrodes were obtained by a conventional three-electrode

system and are compared in Fig. 6c. The Tafel curve is calculated using the formula  $\eta = a + b \log j$ . The Tafel slope of PA@Fe<sub>1/4</sub>-Ni<sub>3</sub>S<sub>2</sub>/NF is 171 mV/decade, which is lower than those of Fe<sub>1/4</sub>-Ni<sub>3</sub>S<sub>2</sub>/NF (252 mV/decade), Fe<sub>1/8</sub>-Ni<sub>3</sub>S<sub>2</sub>/NF (262 mV/decade), Fe<sub>1/10</sub>-Ni<sub>3</sub>S<sub>2</sub>/NF (268 mV/decade), and Ni<sub>3</sub>S<sub>2</sub>/NF (275 mV/decade). The Tafel slope confirms that the reaction kinetics of plasma-modified Fe<sub>1/4</sub>-Ni<sub>3</sub>S<sub>2</sub>/NF toward the HER process are superior to those of pure Fe-Ni<sub>3</sub>S<sub>2</sub>/NF. Then, the  $C_{dl}$  values of the samples was measured to determine the ECSA. The linear relationship between the corresponding current density and different scan rates was plotted, and the  $C_{dl}$  value was obtained by calculating the

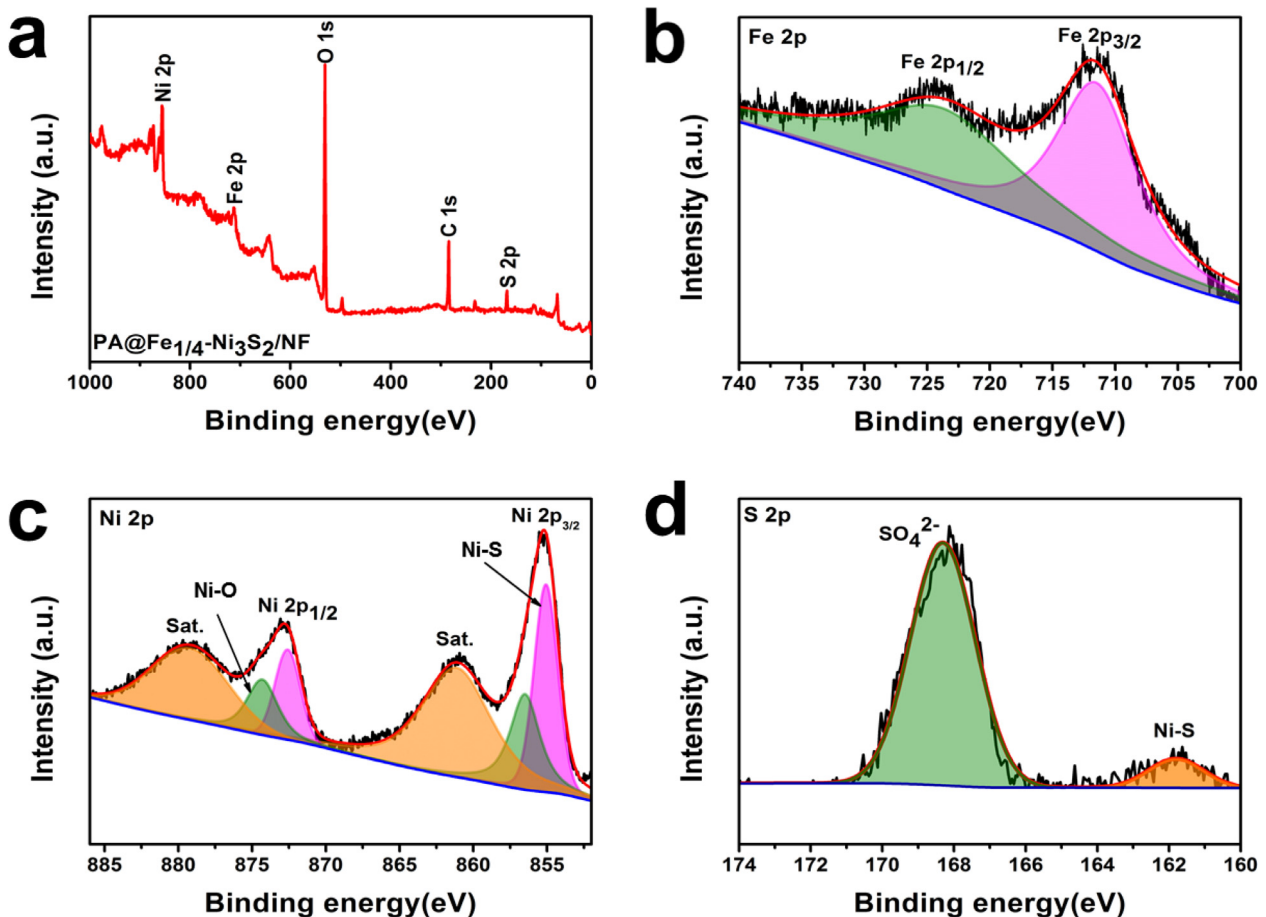


**Fig. 5** (a) XPS survey spectra of PA@Fe<sub>1/4</sub>-Ni<sub>3</sub>S<sub>2</sub>/NF, (b) Fe 2p XPS spectra of PA@Fe<sub>1/4</sub>-Ni<sub>3</sub>S<sub>2</sub>/NF, (c) Ni 2p XPS spectra of PA@Fe<sub>1/4</sub>-Ni<sub>3</sub>S<sub>2</sub>/NF, (d) S 2p XPS spectra of PA@Fe<sub>1/4</sub>-Ni<sub>3</sub>S<sub>2</sub>/NF.

slope of the straight line. As shown in Fig. 6d, PA@Fe<sub>1/4</sub>-Ni<sub>3</sub>S<sub>2</sub>/NF (14.6 mF cm<sup>-2</sup>) also presents the largest  $C_{dl}$  value for HER among three samples, which is 2.0 and 2.9 times those of Fe<sub>1/4</sub>-Ni<sub>3</sub>S<sub>2</sub>/NF (7.2 mF cm<sup>-2</sup>) and Ni<sub>3</sub>S<sub>2</sub>/NF (5.1 mF cm<sup>-2</sup>), respectively, indicating that the PA@Fe<sub>1/4</sub>-Ni<sub>3</sub>S<sub>2</sub>/NF electrode possesses a relatively large ECSA.  $C_{dl}$  is an important indicator used to determine the overall activity of a catalyst (Mishra et al., 2018; Li et al., 2021). PA@Fe<sub>1/4</sub>-Ni<sub>3</sub>S<sub>2</sub>/NF has the largest ECSA of all samples prepared herein, indicating that its enhanced intrinsic activity is attributed to the presence of numerous available active sites and a higher electron transfer rate. Therefore, compared with other catalysts, PA@Fe<sub>1/4</sub>-Ni<sub>3</sub>S<sub>2</sub>/NF has faster reaction kinetics. The results show that plasma modification improves the electrochemical surface area and exposes more active sites, thereby enhancing the HER activity of the catalyst.

EIS (Fig. 7a) was used to better understand the faster catalytic kinetics of PA@Fe<sub>1/4</sub>-Ni<sub>3</sub>S<sub>2</sub>/NF material. According to the Nyquist plot analysis, the charge transfer resistance ( $R_{ct}$ ) of PA@Fe<sub>1/4</sub>-Ni<sub>3</sub>S<sub>2</sub>/NF (2.9 Ω) is substantially smaller than those of Fe<sub>1/4</sub>-Ni<sub>3</sub>S<sub>2</sub>/NF (3.4 Ω), Fe<sub>1/8</sub>-Ni<sub>3</sub>S<sub>2</sub>/NF (3.7 Ω), Fe<sub>1/10</sub>-Ni<sub>3</sub>S<sub>2</sub>/NF (4.3 Ω), and Ni<sub>3</sub>S<sub>2</sub>/NF (11.3 Ω). As was demonstrated, Fe doping increased the electrical conductivity of the material compared to pristine Ni<sub>3</sub>S<sub>2</sub>/NF, and the plasma-modified Fe<sub>1/4</sub>-Ni<sub>3</sub>S<sub>2</sub>/NF nanosheets have the lowest charge transfer resistance, resulting in a higher charge transfer rate.

The increased charge transfer rate is correlated to an increase in the density of the active sites, which is consistent with the ECSA results. To further evaluate the electrochemical stabilities of the PA@Fe<sub>1/4</sub>-Ni<sub>3</sub>S<sub>2</sub>/NF electrode, long-term cyclic voltammogram (CV) cycling tests and i-t curve tests were performed. After the 1000 cycling tests, the LSV curve of the PA@Fe<sub>1/4</sub>-Ni<sub>3</sub>S<sub>2</sub>/NF electrode shows negligible change (Fig. 7b). As shown in Fig. 7b (inset), we explore the long-term stability of the electrocatalyst tested at an overpotential of 200 mV, and find that the current density is nearly constant over 9 h of continuous voltage electrolysis for the HER process. The high electrochemical stability of PA@Fe<sub>1/4</sub>-Ni<sub>3</sub>S<sub>2</sub>/NF is attributed to its durable spherical flower-like 3D nanosheet structure.

In order to understand the intrinsic reasons for the enhanced HER activity of PA@Fe<sub>1/4</sub>-Ni<sub>3</sub>S<sub>2</sub>/NF catalysts, we established a (110) plane-based model to calculate the HER activity of PA@Fe<sub>1/4</sub>-Ni<sub>3</sub>S<sub>2</sub> and Ni<sub>3</sub>S<sub>2</sub> by density functional theory (DFT) method. Electronic structure and adsorption properties. Fig. 8. (a) The side and top views of the (110) surface of PA@Fe<sub>1/4</sub>-Ni<sub>3</sub>S<sub>2</sub>, with yellow, blue, and red spheres representing S, Ni, and Fe atoms, respectively. In general, the free energy of adsorption of H\* on electrocatalysts ( $\Delta G_{H^*}$ ) is considered to be a good description of HER activity (Feng et al., 2015). In general, the free energy of adsorption of H\* on electrocatalysts ( $\Delta G_{H^*}$ ) is considered to be a good description of HER activity. As shown in Fig. 8b, we calculated the active free energies of

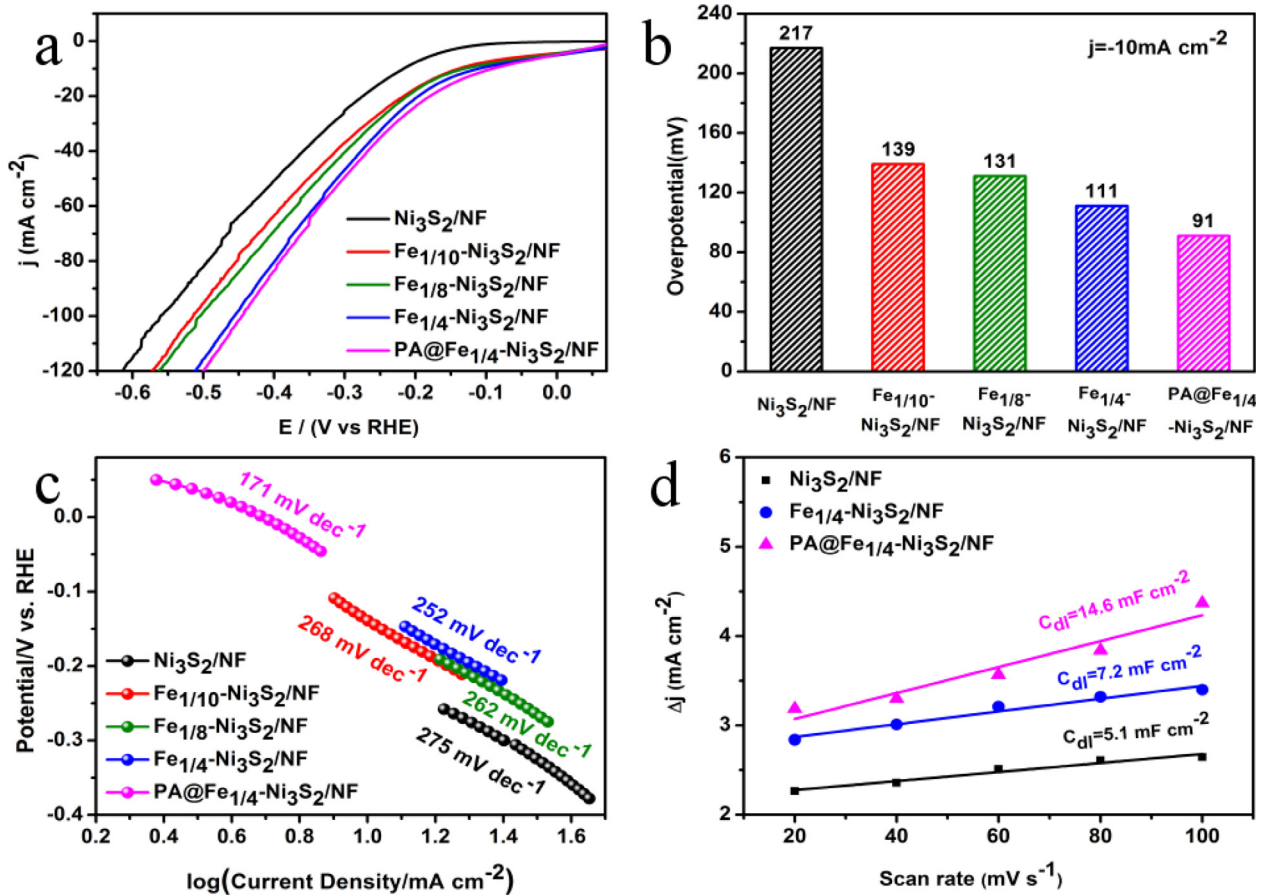


**Fig. 6** Electrochemical HER performance in 1 M KOH: (a) Polarization curves with 85 % iR correction; (b) Comparison of overpotentials for various catalysts at current densities of  $10 \text{ mA cm}^{-2}$  and (c) the Tafel plots. (d) Estimation  $C_{dl}$  of  $\text{Ni}_3\text{S}_2/\text{NF}$ ,  $\text{Fe}_{1/10}\text{-Ni}_3\text{S}_2/\text{NF}$ ,  $\text{Fe}_{1/8}\text{-Ni}_3\text{S}_2/\text{NF}$ ,  $\text{Fe}_{1/4}\text{-Ni}_3\text{S}_2/\text{NF}$ , and  $\text{PA}@ \text{Fe}_{1/4}\text{-Ni}_3\text{S}_2/\text{NF}$  by plotting the current density variation ( $\Delta j = (j_a - j_c)/2$ ).

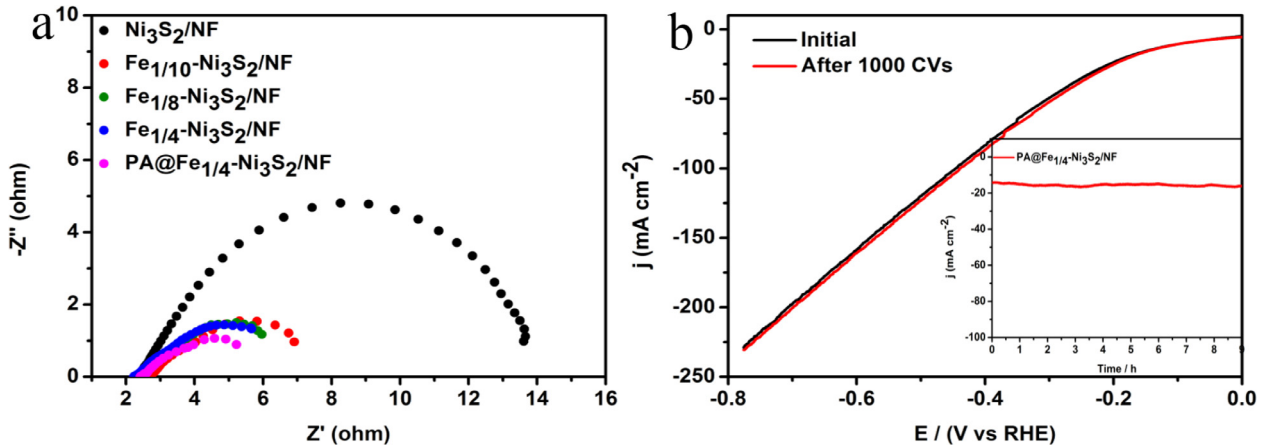


**Fig. 7** (a) Nyquist plots of various catalysts. (b) HER polarization curves of  $\text{PA}@ \text{Fe}_{1/4}\text{-Ni}_3\text{S}_2/\text{NF}$  before and after 1000 CV cycles at a scan rate of  $100 \text{ mV s}^{-1}$ . Inset: Time dependent i-t curves at an overpotential of 200 mV for 10 h.

different sites of  $\text{PA}@ \text{Fe}_{1/4}\text{-Ni}_3\text{S}_2$  and  $\text{Ni}_3\text{S}_2$  catalysts. The calculation results show that the adsorption energy of Ni site of pure  $\text{Ni}_2\text{S}_3$  is 0.86 eV, and the adsorption energy of S site is 0.53 eV, while the adsorption energy of Ni site of  $\text{PA}@ \text{Fe}_{1/4}\text{-Ni}_3\text{S}_2$  is reduced to 0.20 eV, and the adsorption energy of S site is 0.20 eV. Down to 0.10 eV. Obviously, the  $\Delta G_{\text{H}^*}$  of Ni sites and S sites are significantly reduced after plasma doping and

plasma modification. XPS showed that Fe was successfully doped in the  $\text{PA}@ \text{Fe}_{1/4}\text{-Ni}_3\text{S}_2/\text{NF}$  nanosheet arrays and exposed abundant catalytically active sites. Experiments and density functional theory calculations showed that Fe atomic doping and plasma modification reduce the activation energy of the reaction and, thus, enhance the HER activity of the material. Fe– $\text{Ni}_3\text{S}_2$  is the catalytically active site of  $\text{PA}@ \text{Fe}_{1/4}\text{-Ni}_3\text{S}_2/$

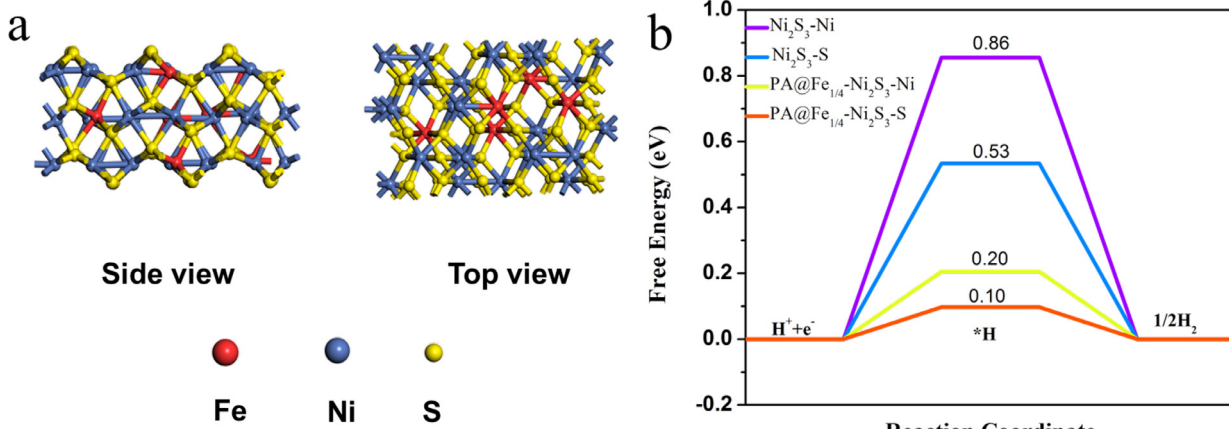


**Fig. 8** (a) Side and Top view of the PA@Fe<sub>1/4</sub>-Ni<sub>3</sub>S<sub>2</sub> (110) surface, the red, blue and yellow spheres represent Fe, Ni and S atoms, respectively. (b) Calculated free-energy diagram of HER over the (110) surfaces of Ni<sub>3</sub>S<sub>2</sub> and PA@Fe<sub>1/4</sub>-Ni<sub>3</sub>S<sub>2</sub>.

NF, which is consistent with data in the literature (Ouyang et al., 2020; Yu et al., 2020).

In summary, the superior HER activity of PA@Fe<sub>1/4</sub>-Ni<sub>3</sub>S<sub>2</sub>/NF may benefit from the following four points: (1) Flower-sphere-like 3D nanosheet structures were grown in situ on nickel foam, exposing abundant active sites and accelerating mass/electron transfer (Huang et al., 2017; Lin et al., 2020); (2) Nanosheet arrays provide high electrochemical surface area for catalysts; (3) Fe atom doping optimizes the electronic structure, enhances the electron transport rate and improves the intrinsic activity of PA@Fe<sub>1/4</sub>-Ni<sub>3</sub>S<sub>2</sub>/NF nanosheets; and (4) Plasma modification disperses the agglomerated nanosheets, which further increases the electrochemical surface area and active sites to accelerate the reaction kinetics and improve the catalytic performance.

#### 4. Conclusions

In conclusion, we successfully synthesized Fe-doped Ni<sub>3</sub>S<sub>2</sub> nanosheets (Fe-Ni<sub>3</sub>S<sub>2</sub>/NF) on nickel foam via a two-step hydrothermal method. Electrochemical test results show that optimal catalytic activity is obtained when the Fe/Ni molar ratio is 1:4. After plasma modification, PA@Fe<sub>1/4</sub>-Ni<sub>3</sub>S<sub>2</sub>/NF has a unique spherical flower-like nanosheet structure and high catalytic performance and long-term stability in alkaline solutions. As expected, an overpotential of only 91 mV was required to drive the HER reaction at a current density of 10 mA cm<sup>-2</sup>. In addition, the catalyst exhibits long-term stability in alkaline solution. This is mainly because Fe doping enhances the intrinsic activity of Ni<sub>3</sub>S<sub>2</sub> and optimizes the electronic structure as well as plasma modification to further increase the electrochemical surface area and active sites. This study confirms the feasibility of developing high-efficiency water-splitting electrocatalysts through a combination of elemental doping and plasma modification strategies. Based on the obtained results, a future research direction is to develop HER catalysts superior to noble-metal-based catalysts by optimizing the plasma-modification conditions and devices, and doping with different non-precious metals.

#### Declaration of competing interest

The authors declare that they have no known competing financial interests or personal relationships that could have appeared to influence the work reported in this paper.

#### Acknowledgments

The authors gratefully acknowledged the financial support from National Natural Science Foundation of China (No. 21246010), Science and Technology Project Fund of Nantong (JC2021163), the Key Natural Science Foundation of the Jiangsu Higher Education Institutions of China (Grant No. 22KJA610001) and Changzhou Institute of Technology High level Talent Launch Project (YN22010).

#### References

- Ahmed, T., Asghar, M.A., Ali, A., Akhter, Z., Ali, S., Ullah, I., Nisar, T., Wagner, V., Touseef, S., Hussain, A., Haider, A., 2022. High-nuclearity cobalt(II)-containing polyoxometalate anchored on nickel foam as electrocatalyst for electrochemical water oxidation studie. *J. Alloys Compd.* 909, 164709.
- Anantharaj, S., Ede, S.R., Karthick, K., Sankar, S.S., Sangeetha, K., Karthik, P.E., Kundu, S., 2018. Precision and correctness in the evaluation of electrocatalytic water splitting: revisiting activity parameters with a critical assessment. *Energy Environ. Sci.* 11, 744–771.
- Biesinger, M.C., Payne, B.P., Lau, L.W.M., Gerson, A., Smart, R.S. C., 2009. X-ray photoelectron spectroscopic chemical state quantification of mixed nickel metal, oxide and hydroxide systems. *Surf. Interface Anal.* 41, 324–332.
- Chen, M., Liu, J.-B., Kitiphatpiboon, N., Li, X.-M., Wang, J.-L., Hao, X.-G., Abudula, A., Ma, Y.-F., Guan, G.Q., 2022. Zn-VO<sub>x</sub>-Co nanosheets with amorphous / crystalline heterostructure for highly efficient hydrogen evolution reaction. *Chem. Eng. J.* 432, (15) 134329.
- Chen, Y.-B., Zhang, X.-Y., Qin, J.-Q., Liu, R.-P., 2021a. Transition metal atom doped Ni<sub>3</sub>S<sub>2</sub> as efficient bifunctional electrocatalysts for overall water splitting: design strategy from DFT studies. *Mol. Catal.* 516, 111955.
- Chen, Y.-P., Zhao, Q.-C., Yao, Y.-L., Li, T.-H., 2021b. The preparation of ionic liquid based iron phosphate/CNTs composite via microwave radiation for hydrogen evolution reaction and oxygen evolution reaction. *Arab. J. Chem.* 14, 103440.
- Cheng, N.-Y., Liu, Q., Asiri, A.M., Xing, W., Sun, X.-P., 2015. A Fe-doped Ni<sub>3</sub>S<sub>2</sub> particle film as a high-efficiency robust oxygen evolution electrode with very high current density. *J. Mater. Chem. A* 3, 23207–23212.

- Dueso, C., Izquierdo, M.T., Labiano, F.G., Diego, L.F., Abad, A., Gayán, P., Adámez, J., 2012. Effect of H<sub>2</sub>S on the behaviour of an impregnated NiO-based oxygencarrier for chemical-looping combustion (CLC). *Appl. Catal. B*. 126, 186–199.
- Feng, L.-L., Fan, M.-H., Wu, Y.-Y., Liu, Y.-P., Li, G.-D., Chen, H., Chen, W., Wang, D.-J., Zou, X.-X., 2016. Metallic Co<sub>9</sub>S<sub>8</sub> nanosheets grown on carbon cloth as efficient binder-free electrocatalysts for the hydrogen evolution reaction in neutral media. *J. Mater. Chem. A*. 4, 6860–6867.
- Feng, Z.-P., Sui, Y.-W., Sun, Z., Qi, J.-Q., Wei, F.-X., Ren, Y.-J., Zhan, Z.-Z., Zhou, M.-H., Meng, D.-M., Zhang, L.-J., Ma, L., Wang, Q., 2021. Controllable synthesis of flower-like Mn-Co-P nanosheets as bifunctional electrocatalysts for overall water splitting. *Colloids Surf. A Physicochem. Eng. Aspects* 615.
- Feng, L.-L., Yu, G.-T., Wu, Y.-Y., Li, G.-D., Li, H., Sun, Y.-H., Asefa, T., Chen, W., Zou, X.-X., 2015. High-index faceted Ni3S2 nanosheets arrays as highly active and ultrastable electrocatalysts for water splitting. *J. Am. Chem. Soc.* 137, 14023–14026.
- Guo, W.-H., Zhang, Q., Fu, H.-C., Yang, Y.-X., Chen, X.-H., Luo, H.-Q., 2022. Semi-sacrificial template growth of FeS/Fe<sub>2</sub>O<sub>3</sub> heterogeneous nanosheets on iron foam for efficient oxygen evolution reaction. *J. Alloys Compd.* 909, 164670.
- Hao, S., Cao, Q., Yang, L.-T., Che, R.-C., 2020. Morphology-optimized interconnected Ni<sub>3</sub>S<sub>2</sub> nanosheets coupled with Ni(OH)<sub>2</sub> nanoparticles for enhanced hydrogen evolution reaction. *J. Alloys Compd.* 827, 154163.
- Huang, H.-W., Yu, C., Zhao, C.-T., Han, X.-T., Yang, J., Liu, Z.-B., Li, S.-F., Zhang, M.-D., Qiu, J.-S., 2017. Iron-tuned super nickel phosphide microstructures with high activity for electrochemical overall water splitting. *Nano Energy* 34, 472–480.
- Irshad, A., Munichandraiah, N., 2017. Electrodeposited nickel-cobalt-sulfide catalyst for the hydrogen evolution reaction. *ACS Appl. Mater. Interfaces*. 9, 19746–19755.
- Jia, L., Du, G.H., Han, D., Hao, Y., Zhao, W.Q., Fan, Y., Su, Q.M., Dinga, S.K., Xu, B.S., 2021. Ni<sub>3</sub>S<sub>2</sub>/Cu–NiCo LDH heterostructure nanosheet arrays on Ni foam for electrocatalytic overall water splitting. *9* (48), 27639–27650.
- Jian, J., Yuan, L., Qi, H., Sun, X.-J., Zhang, L., Li, H., Yuan, H.-M., Feng, S.-H., 2018. Sn-Ni<sub>3</sub>S<sub>2</sub> ultrathin nanosheets as efficient bifunctional water splitting catalyst with large current density and low overpotential. *ACS Appl. Mater. Interfaces* 10, 40568–40576.
- Jin, H.-Y., Liu, X., Chen, S.-M., Vasileff, A., Li, L.-Q., Jiao, Y., Song, L., Zheng, Y., Qiao, S.-Z., 2019. Heteroatom-doped transition metal electrocatalysts for hydrogen evolution reaction. *ACS Energy Lett.* 4, 805–810.
- Jin, Q.-Y., Ren, B.-W., Li, D.-Q., Cui, H., Wang, C.-X., 2017. Plasma-assisted synthesis of self-supporting porous CoNPs@C nanosheet as efficient and stable bifunctional electrocatalysts for overall water splitting. *ACS Appl. Mater. Interfaces* 9, 31913–31921.
- Karthick, K., Anantharaj, S., Karthik, P.E., Subramanian, B., Kundu, S., 2017. Self-assembled molecular hybrids of CoS-DNA for enhanced water oxidation with low cobalt content. *Inorg. Chem.* 56, 6734–6745.
- Kim, H.S., Cook, J.B., Lin, H., Ko, J.S., Tolbert, S.H., Ozolins, V., Dunn, B., 2017. Oxygen vacancies enhance pseudocapacitive charge storage properties of MoO<sub>3-x</sub>. *Nat. Mater.* 16, 454–460.
- Lee, Y.J., Park, S.K., 2022. Metal-organic framework-derived hollow cosx nanoarray coupled with nife layered double hydroxides as efficient bifunctional electrocatalyst for overall water splitting. *Small* 18, 2200586.
- Li, F., Chen, J.X., Zhang, D.F., Fu, W.F., Chen, Y., Wen, Z.H., Lv, X.J., 2013. Heteroporous MoS<sub>2</sub>/Ni3S<sub>2</sub> towards superior electrocatalytic overall urea splitting. *Chem. Commun.* 54 (41), 5181–5184.
- Li, D., Li, Y., Zhang, B.-W., Lui, Y., Mooni, S., Chen, R.-S., Hu, S., Ni, H.-W., 2018. Insertion of platinum nanoparticles into MoS<sub>2</sub> nanoflakes for enhanced hydrogen evolution reaction. *Materials* 11, 1520.
- Li, D.-Y., Liao, L.-L., Zhou, H.-Q., Zhao, Y., Cai, F.-M., Zeng, J.-S., Liu, F., Wu, H., Tang, D.-S., Yu, F., 2021. Highly active non-noble electrocatalyst from Co<sub>2</sub>P/Ni<sub>2</sub>P nanohybrids for pH-universal hydrogen evolution reaction. *16*, 100314.
- Li, T., Liu, Y.-D., Huang, S.-S., Jia, R.-R., Shi, L.-Y., Huang, L., 2022b. Photochemical fabrication of bimetal wormlike heterostructured nanorods for enhanced electrochemical hydrogen evolution reaction. *J. Alloys Compd.* 910, 164913.
- Li, J.-Q., Zhang, B.-Y., Song, Q.-Q., Xu, X.-T., Hou, W.-F., 2020. Sulfur and molybdenum Co-doped graphitic carbon nitride as a superior water dissociation electrocatalyst for alkaline hydrogen evolution reaction. *Ceram. Int.* 46, 14178–14187.
- Li, J.-Y., Zhao, M., Yi, L.-Y., Feng, B.-M., Fang, C.-X., Peng, Z.-P., Hu, W.-H., 2022a. Sacrificial templating synthesis of metal-organic framework hybrid nanosheets as efficient pre-electrocatalyst for oxygen evolution reaction in alkaline. *Colloids Surf. A Physicochem. Eng. Aspects* 632, 127745.
- Liang, H.-F., Gandi, A.N., Anjum, D.H., Wang, X.-B., Schwingenschlögl, U., Alshareef, H.N., 2016. Plasma-assisted synthesis of NiCoP for efficient overall water splitting. *Nano Lett* 16, 7718–7725.
- Lin, J.-H., Yan, Y.-T., Xu, T.-X., Qu, C.-Q., Li, J., Cao, J., Feng, J.-C., Qi, J.-L., 2020. S doped NiCo<sub>2</sub>O<sub>4</sub> nanosheet arrays by Ar plasma: an efficient and bifunctional electrode for overall water splitting. *J. Colloid Interface Sci.* 560, 34–39.
- Liu, C., Li, F., Xue, S., Lin, H., Sun, Y., Cao, J., Chen, S., 2021. Fe Doped Ni<sub>3</sub>S<sub>2</sub> Nanosheet Arrays for Efficient and Stable Electrocatalytic Overall Urea Splitting. *ACS Appl. Energy Mater.* 5 (1), 1183–1192.
- Lu, F., Zhou, M., Li, W.-R., Weng, Q.-H., Li, C.-L., Xue, Y.-M., Jiang, X.-F., Zeng, X.-H., Bando, Y., Golberg, D., 2016. Engineering sulfur vacancies and impurities in NiCo<sub>2</sub>S<sub>4</sub> nanostructures toward optimal supercapacitive performance. *Nano Energy* 26, 313–323.
- Ma, L.-Z., Zhang, K., Wang, S., Gao, L.-N., Sun, Y.-F., Liu, Q.-Y., Guo, J.-X., Zhang, X., 2019. Vanadium doping over Ni<sub>3</sub>S<sub>2</sub> nanosheet array for improved overall water splitting. *Appl. Surf. Sci.* 489, 815–823.
- Mishra, I.K., Zhou, H.-Q., Sun, J.-Y., Dahal, K., Chen, S., Ren, Z.-F., 2018. Hierarchical CoP/Ni<sub>3</sub>P<sub>4</sub>/CoP microsheet arrays as a robust pH universal electrocatalyst for efficient hydrogen generation. *Energy Environ. Sci.* 11, 2246.
- Mooni, S.P., Kondamareddy, K.K., Li, S., Zhou, X., Chang, L., Ke, X., Yang, X.Q., Li, D., Qu, Q., 2020. Graphene oxide decorated bimetal (MnNi) oxide nanoflakes used as an electrocatalyst for enhanced oxygen evolution reaction in alkaline media. *Arab. J. Chem.* 13, 4553–4563.
- Ouyang, T., Wang, X.T., Mai, X.Q., Chen, A.N., Tang, Z.Y., Liu, Z.-Q., 2020. Coupling Magnetic Single-Crystal Co<sub>2</sub>Mo<sub>3</sub>O<sub>8</sub> with Ultrathin Nitrogen-Rich Carbon Layer for Oxygen Evolution Reaction. *Angew. Chem. Int. Ed.* 59, 11948–11957.
- Pu, Z., Luo, Y.-L., Asiri, A.M., Sun, X.-P., 2016. Efficient electrochemical water splitting catalyzed by electrodeposited nickel diselenide nanoparticles based film. *ACS Appl. Mater. Interfaces* 8, 4718–4723.
- Santo, H.L.S., Corradin, P.G., Medina, M., Dias, J.A., Mascaro, L.H., 2020. NiMo-NiCu inexpensive composite with high activity for hydrogen evolution reaction. *ACS Appl. Mater. Interfaces* 12, 17492–17501.
- Shen, Y.-J., Wang, Y.-L., Fan, K.-X., 2019. Application of CuO/AC in DBD plasma for dye wastewater treatment: synthesis, optimization, and coupling mechanism. *Desal. Wat. Treat.* 138, 173–182.
- Shi, M.-Y., Sun, X.-C., Bai, Q., Zhang, Y., Yu, S.-S., Liu, M.-H., Wang, L., Yu, W.-W., Sui, N., 2022. Graphdiyne/graphene heterostructure supported NiFe layered double hydroxides for

- oxygen evolution reaction. *Colloids Surf. A Physicochem. Eng. Aspects* 637, 128217.
- Suen, N.T., Hung, S.F., Quan, Q., Zhang, N., Xu, Y.-J., Chen, H.-M., 2017. Electrocatalysis for the oxygen evolution reaction: recent development and future perspectives. *Chem. Soc. Rev.* 46, 337–365.
- Sultana, F., Mushtaq, M., Wang, J.-H., Althubeiti, K., Zaman, A., Rais, A.K., Ali, A., Yang, Q., 2022. An insight to catalytic synergic effect of Pd-MoS<sub>2</sub> nanorods for highly efficient hydrogen evolution reaction. *Arab. J. Chem.* 15, 103735.
- Tang, C., Zhang, R., Lu, W., He, L., Jiang, X., Asiri, A.M., Sun, X., 2017. Fe-doped CoP nanoarray: a monolithic multifunctional catalyst for highly efficient hydrogen generation. *Adv. Mater.* 29, 1602441.
- Wang, H.-H., Ai, T.-T., Bao, W.-W., Zhang, J.-J., Wang, Y., Kou, L.-J., Li, W.-H., Deng, Z.-F., Song, J.-J., Li, M., 2021. Regulating the electronic structure of Ni<sub>3</sub>S<sub>2</sub> nanorods by heteroatom vanadium doping for high electrocatalytic performance. *Electrochim. Acta* 395, 139180.
- Wang, X.-Y., Yuan, G.-J., Bai, J.-L., Zhang, L., Zhua, Y.-Q., Wu, S., Ren, L.-L., 2022. Modulating electronic structure of Ni<sub>2</sub>P precatalyst by doping trace iron for enhanced oxygen evolution reaction in alkaline. *J. Alloys Compd.* 908, 164603.
- Wang, Y.-Y., Zhang, Y.-Q., Liu, Z.-J., Xie, C., Feng, S., Liu, D.-D., Shao, M.-F., Wang, S.-Y., 2017. Layered double hydroxide nanosheets with multiple vacancies obtained by dry exfoliation as highly efficient oxygen evolution electrocatalysts. *Angew. Chem. Int. Ed.* 56, 5867–5871.
- Wang, L., Zhang, B.-B., Rui, Q., 2018. Plasma-induced vacancy defects in oxygen evolution cocatalysts on TA<sub>3</sub>N<sub>5</sub> photoanodes promoting solar water splitting. *ACS Catal.* 8, 10564–10572.
- Xie, J.-Y., Li, C., Niu, J.-A., Zhang, S.-H., Ou, X.-M., Feng, P.-Z., Garcia, H., 2021. Porous NiFe-LDH grown on graphene oxide towards highly efficient OER electrocatalysis. *Mater. Lett.* 290, 129517.
- Xing, Z.-C., Wang, D.-W., Meng, T., Yang, X.-R., 2020. Superb hydrogen evolution by Pt nanoparticles decorated Ni<sub>3</sub>S<sub>2</sub> microrods array. *ACS Appl. Mater. Interfaces* 12, 39163–39169.
- Xu, X.-M., Chen, Y.-B., Zhou, W., Zhu, Z.-H., Su, C., Liu, M.-L., Shao, Z.-P., 2016a. A perovskite electrocatalyst for efficient hydrogen evolution reaction. *Adv. Mater.* 28, 6442–6448.
- Xu, Q.-H., Fang, S.-K., Chen, Y., Park, J.-K., Pan, C., Shen, Y.-J., Zhu, N., Wu, H.-F., 2021. Synergistic photocatalytic activity of a combination of carbon nanotubes-graphene-nickel foam nanocomposites enhanced by dielectric barrier discharge plasma technology for water purification. *Water Sci. Technol.* 83, 2762–2777.
- Xu, H., Fei, B., Cai, G., Ha, Y., Liu, J., Jia, H., Zhang, J., Liu, M., Wu, R., 2020. Boronization-induced ultrathin 2D nanosheets with abundant crystalline-amorphous phase boundary supported on nickel foam toward efficient water splitting. *Adv. Energy Mater.* 10, 1902714.
- Xu, X., Song, F., Hu, X.-L., 2016b. A nickel iron diselenide-derived efficient oxygen-evolution catalyst. *Nat. Commun.* 7, 12324.
- Yang, Y., Luan, X.-B., Dai, X.-P., Zhang, X., Qiao, H.-Y., Zhao, H.-H., Yong, J.-X., Yu, L., Han, J.-H., Zhang, J., 2019. Partially sulfurated ultrathin nickel-iron carbonate hydroxides nanosheet boosting the oxygen evolution reaction. *Electrochim. Acta* 309, 57–64.
- Yu, L., Zhou, H.-Q., Sun, J.-Y., Qin, F., Yu, F., Bao, J.-M., Yu, Y., Chen, S., Ren, Z.-F., 2017. Cu nanowires shelled with NiFe layered double hydroxide nanosheets as bifunctional electrocatalysts for overall water splitting. *Energy Environ. Sci.* 10 (8), 1820–1827.
- Yu, L., Wu, L.-B., McElhenny, B., Song, S.-W., Luo, D., Zhang, F.-H., Yu, Y., Chen, S., Ren, Z.-F., 2020. Ultrafast room-temperature synthesis of porous S-doped Ni/Fe (oxy)hydroxide electrodes for oxygen evolution catalysis in seawater splitting. *Energy Environ. Sci.* 13, 3439–3446.
- Yuan, C.-Z., Sun, Z.-T., Jiang, Y.-F., Yang, Z.-K., Jiang, N., Zhao, Z.-W., Qazi, U.-Y., Zhang, W.-H., Xu, A.-W., 2017. One-step in situ growth of iron-nickel sulfide nanosheets on FeNi alloy foils: high-performance and self-supported electrodes for water oxidation. *Small* 13, 1604161.
- Zhang, G., Feng, Y.-S., Lu, W.-T., He, D., Wang, C.-Y., Li, Y.-K., Wang, X.-Y., Cao, F.-F., 2018b. Enhanced catalysis of electrochemical overall water splitting in alkaline media by Fe doping in Ni<sub>3</sub>S<sub>2</sub> nanosheet arrays. *ACS Catal.* 8, 5431–5441.
- Zhang, H., Jiang, H., Hu, Y., Saha, P., Li, C., 2018c. Mo-triggered amorphous Ni<sub>3</sub>S<sub>2</sub> nanosheets as efficient and durable electrocatalysts for water splitting. *Mater. Chem. Front.*
- Zhang, H.-X., Jiang, H., Hu, Y.-J., Saha, P., Li, C.-Z., 2018d. Mo-triggered amorphous Ni<sub>3</sub>S<sub>2</sub> nanosheets as efficient and durable electrocatalysts for water splitting. *Mater. Chem. Front.* 2, 1462–1466.
- Zhang, A.-T., Li, A.-H., Zhao, W., Yan, G.-W., Liu, B.-P., Liu, M.-L., Li, M.-X., Huo, B.-B., Liu, J.-Q., 2018a. An efficient and self-guided chemo-photothermal drug loading system based on copolymer and transferrin decorated MoS<sub>2</sub> nanodots for dually controlled drug release. *Chem. Eng. J.* 342, 120–132.
- Zhang, W., Li, D.-H., Zhang, L.-Z., She, X.-L., Yang, D.-J., 2019. NiFe-based nanostructures on nickel foam as highly efficiently electrocatalysts for oxygen and hydrogen evolution reactions. *J. Energy Chem.* 39, 39–53.
- Zhang, H.-J., Maijenburg, A.W., Li, X.-P., Schweizer, S.L., Wehrspohn, R.B., 2020. Bifunctional heterostructured transition metal phosphides for efficient electrochemical water splitting. *Adv. Funct. Mater.* 30, 2003261.
- Zhang, T., Wu, M., Yan, D., Mao, J., Liu, H., Hu, W., Du, X., Ling, T., Zhang, S., 2018g. Engineering oxygen vacancy on NiO nanorod arrays for alkaline hydrogen evolution. *Nano Energy* 43, 103–109.
- Zhang, K., Zhang, G., Qu, J.-H., Liu, H.-J., 2018e. Tungsten-assisted phase tuning of molybdenum carbide for efficient electrocatalytic hydrogen evolution. *ACS Appl. Mater. Inter.* 10, 2451–2459.
- Zhang, R.-R., Zhang, Y.-C., Pan, L., Shen, G.-Q., Mahmood, N., Ma, Y.-H., Shi, Y., Jia, W., Wang, L., Zhang, X., Xu, W., Zou, J.-J., 2018f. Engineering cobalt defects in cobalt oxide for highly efficient electrocatalytic oxygen evolution. *ACS Catal.* 8, 3803–3811.
- Zhao, L., Guo, Z.-A., Liu, Z.-F., 2022. Facile synthesis and efficient electrochemical water splitting of bifunctional nanostructured Ni-based layered double hydroxide/sulfide composite. *J. Alloys Compd.* 910, 164880.
- Zheng, X.-R., Han, X.-P., Zhang, Y.-Q., Wang, J.-H., Zhong, C., Deng, Y.-D., Hu, W.-B., 2019. Controllable synthesis of nickel sulfide nanocatalysts and their phase-dependent performance for overall water splitting. *Nanoscale* 11, 5646–5654.
- Zheng, Y.-W., Wang, X.-X., Zhao, W., Cao, X.-Y., Liu, J.-Q., 2018. Phytic acid-assisted synthesis of ultrafine NiCo<sub>2</sub>S<sub>4</sub> nanoparticles immobilized on reduced graphene oxide as high-performance electrode for hybrid supercapacitors. *Chem. Eng. J.* 333, 603–612.
- Zhou, Y., Zhang, J.-T., Sun, F.-C., Yu, X.-P., Kang, W.-P., Zhang, J., 2020. One-step synthesis of Co<sub>9</sub>S<sub>8</sub>@Ni<sub>3</sub>S<sub>2</sub> heterostructure for enhanced electrochemical performance as sodium ion battery anode material and hydrogen evolution electrocatalyst. *J. Solid State Chem.* 285, 121230.
- Zhu, Y.-F., Xu, G.-Y., Song, W.-Q., Zhao, Y.-Z., Hea, Z., Miao, Z.-C., 2021. Anchoring single Ni atoms on defected 2D MXene nanosheets as an efficient electrocatalyst for enhanced hydrogen evolution reaction. *Ceram. Int.* 47, 30005–30011.